ELSEVIER

Chemical Engineering Journal 86 (2002) 117–131

Chemical Engineering Journal

www.elsevier.com/locate/cej

A heterogeneous wood drying computational model that accounts for material property variation across growth rings

P. Perré [a,*], I.W. Turner [b]

[a] *LERMAB, Laboratory of Wood Sciences, UMR INRA 1093, ENGREF, 14 rue Girardet, F-54042 Nancy Cedex, France*
[b] *School of Mathematical Sciences, Queensland University of Technology, G.P.O. Box 2434, Brisbane Q4001, Australia*

Abstract

In this work, a comprehensive two-dimensional drying model, known as TransPore, is extended so that the effect of material heterogeneity and local material directions on the heat and mass transport processes evolving within the medium can be investigated. The underlying mathematical theory enables the property variations as well as the spatial changes of local material directions to be taken into consideration throughout the computation. The model, which enables the behaviour of the moisture content, internal temperature and pressure fields to be monitored during the drying process, uses a control-volume finite-element (CV-FE) formulation, together with a suite of sophisticated numerical techniques to ensure both accurate and efficient simulation results.

A board section of softwood is used to depict the possibilities offered by this model. In this case, the material directions vary along the section according to the pith position that defines the radial and tangential directions. In addition, the material properties change significantly from earlywood to latewood. A comparison of the overall drying kinetics generated by both the heterogeneous and the classical homogeneous models will provide a clear understanding of the impact and importance of treating the local wood properties when drying softwood.

Keywords: Globally convergent Newton method; Flux limiting; Control-volume finite-element method; Heterogeneous; Anisotropic

1. Introduction

Wood is a fascinating biological porous material that is both anisotropic and heterogeneous. Its structure is rather complex, however, it is well known and thoroughly documented in the literature (see, e.g. [1]). The cell wall thickness varies considerably from earlywood to latewood across a growth ring and the density is higher in latewood in comparison to earlywood. In fact, the density variation across a growth ring of a tree can range between a factor of 3 and 4 for wood elaborated in spring as compared to wood elaborated in late summer. Clearly, as a result of this variation, almost all of the physical properties of wood depend strongly on the position within the annual ring and this density variation must be taken into consideration when developing a mathematical model that describes the drying of softwood. It is the primary aim of this paper to study in detail the effects of heterogeneity on the drying of a sample of wood modelled at the scale of the annual growth increment.

Recently, some research work has focussed on the development of mathematical models that treat the heterogeneity evident in wood [2–6]. In particular, the two-dimensional model proposed by Plumb and Gong for the radial and tangential wood directions predicted the variations in moisture content across the growth ring that were observed experimentally. Further, it was seen that the earlywood exposed at the drying surface dries quickly during the early stages of drying and that the free water tended to move diagonally across the sample due to the high permeability in the radial direction. All of these effects were evident during the experiment.

In this work, a comparison of the overall drying kinetics generated by a new heterogeneous drying model and a classical homogeneous model [7] for high temperature drying will be presented. The majority of this paper concerns the detailed discussion of the new heterogeneous drying model and the sophisticated numerical techniques that ensure that the simulation results are accurate and that the computations are performed efficiently. This new model supersedes the previous versions of the computational code TransPore. Here, a completely unstructured mesh built by tessellating the solution domain with triangles is used for the virtual board description. Thereafter, a control-volume finite-element (CV-FE) discretisation process is performed to transform the non-linear partial differential system that

* Corresponding author. Fax: +33-383-399-6847.
E-mail address: perre@engref.fr (P. Perré).

1385-8947/02/$ – see front matter
PII: S1385-8947(01)00270-4

Nomenclature

$\boldsymbol{J}$	flux vector (kg m^{-2} s^{-1})
$\overline{\overline{\boldsymbol{K}}}$	kinetic transport tensor
S	saturation
t	time (s)
T	temperature (K)
$\boldsymbol{v}$	velocity (m s^{-1})
X	moisture content dry basis

Greek letters

ϕ	porosity
φ	phase potential
ρ	intrinsic averaged density (kg m^{-3})
ω	mass fraction
Ψ	conserved quantity

Subscripts

a	air
b	bound water
eff	effective property
g	gas phase
v	vapour phase
w	liquid phase

describes the drying process into a discrete non-linear algebraic system analogue.

2. Mathematical formulation

2.1. The heterogeneous transport model

The macroscopic equations that govern heat and mass transport in a homogeneous porous medium have been discussed in great detail previously by Whitaker [8,9]. These equations also have been used with great success to model the drying of a homogeneous sample of wood (consisting of either all sapwood or all heartwood) for several different drying configurations [10–12]. In this work, these equations have been extended to account for material heterogeneity through the apparent density of the porous medium $\rho_0(\boldsymbol{x})$ and via the density variation of the material properties, capillary pressure, permeability, diffusivity and conductivity. The mathematical model is summarised briefly as follows.

Liquid conservation:

$$\frac{\partial}{\partial t}(\rho_0(\boldsymbol{x})X + \varepsilon_g\rho_v) + \nabla\cdot(\rho_w\bar{\boldsymbol{v}}_w + \rho_v\bar{\boldsymbol{v}}_g + \overline{\rho_b\boldsymbol{v}_b}) = \nabla\cdot(\rho_g\overline{\overline{\boldsymbol{D}}}_{eff}\nabla\omega_v) \quad (1)$$

Air conservation:

$$\frac{\partial}{\partial t}(\bar{\rho}_a) + \nabla\cdot(\rho_a\bar{\boldsymbol{v}}_g) = \nabla\cdot(\rho_g\overline{\overline{\boldsymbol{D}}}_{eff}\nabla\omega_a) \quad (2)$$

Energy conservation:

$$\frac{\partial}{\partial t}\left(\rho_0(\boldsymbol{x})(Xh_w + h_s) + \varepsilon_g(\rho_v h_v + \rho_a h_a) - \int_0^{\bar{\rho}_b}\Delta h_w\,d\rho - \varepsilon_g P_g\right) + \nabla\cdot(\rho_w h_w\bar{\boldsymbol{v}}_w + (\rho_v h_v + \rho_a h_a)\bar{\boldsymbol{v}}_g + h_b\overline{\rho_b\boldsymbol{v}_b}) = \nabla\cdot(\bar{\rho}_g\overline{\overline{\boldsymbol{D}}}_{eff}(h_v\nabla\omega_v + h_v\nabla\omega_a) + \overline{\overline{\boldsymbol{K}}}_{eff}\nabla T) \quad (3)$$

The gas and liquid phase velocities are given by the generalised Darcy's law:

$$\bar{\boldsymbol{v}}_\ell = -\frac{\overline{\overline{\boldsymbol{K}}}_\ell\overline{\overline{\boldsymbol{k}}}_\ell}{\mu_\ell}\nabla\varphi_\ell, \qquad \nabla\varphi_\ell = \nabla P_\ell - \rho_\ell g\nabla\chi, \quad \text{where } \ell = w, g \quad (4)$$

The quantities φ are known as the phase potentials and χ is the depth scalar. All other symbols have their usual meaning. The bound liquid flux is assumed to proportional to a gradient in the bound water moisture content:

$$\overline{\rho_b\boldsymbol{v}_b} = -\rho_0(\boldsymbol{x})\overline{\overline{\boldsymbol{D}}}_b\nabla X_b \quad (5)$$

2.2. Closure conditions

Because wood is a highly hygroscopic porous medium, bound liquid must be separated from free water in the definition of moisture content:

$$X = X_w + X_b \equiv \frac{\varepsilon_w\rho_w}{\rho_0} + \min(X, X_{FSP}), \quad X_{FSP} = 0.325 - 0.001T \quad (6)$$

The volume fractions of the liquid and gaseous phases are defined, in the usual sense, as $\varepsilon_w = \phi S_w$, $\varepsilon_g = \phi(1 - S_w)$, $\varepsilon_w + \varepsilon_g = \phi$. The intrinsic phase air density is defined as $\bar{\rho}_a = \varepsilon_g\rho_a$ and the gaseous phase is a binary mixture of air and vapour, which is assumed to behave like an ideal gas. During drying both liquid and gaseous phases are evident within the porous medium. As a result of the curvature of the interface that exists between the liquid and the gas phases within the pores of the medium, the liquid pressure is less than the gas pressure and the capillary pressure represents that difference:

$$P_w = P_g - P_c \quad (7)$$

The mass fractions of the air and vapour phases are defined by ω_a and ω_v, respectively.

2.3. Boundary and initial conditions

The boundary conditions have been discussed in great detail previously (see, e.g. [11,12]). For the wood sample under consideration here, only one half of the sample is computed and all fluxes of liquid, vapour, air and heat are assumed zero at the symmetry plane. Initially, the porous medium

has some prescribed uniform temperature distribution and the pressure is constant throughout at the atmospheric value. The initial moisture content field must be determined by solving a non-linear system that involves an equilibration of capillary forces throughout the medium, together with the requirement that an overall mass balance equation be satisfied.

2.4. Material properties

Recent research has been focussed on determining the material property variations across a growth ring of softwood [7,13]. In that work, experimental observation and mathematical tools including image analysis, homogenisation and a simple tracheid model enabled a complete set of correlations for capillary pressure $P_c(\rho_0, X_w, T)$, bound liquid diffusivity $\overline{\overline{D}}_b(\rho_0, X_b, T)$, thermal conductivity $\overline{\overline{K}}_{eff}(\rho_0, X, T)$ and absolute permeability $\overline{\overline{k}}_w(\rho_0), \overline{\overline{k}}_g(\rho_0)$ to be postulated. These properties have been used for the simulation results discussed throughout this text and the interested reader is referred to the reference papers for further details on the exact form of the correlations.

2.5. Mesh generation and treatment of the wood grain angle

When a board is cut from a log (cf. Fig. 1) the grain angle needs to be taken into consideration for the material property tensor terms that are evident in the transport Eqs. (1)–(5). For a homogeneous porous media model, the anisotropy of the system is assumed to be in the direction of the principal axes of a Cartesian co-ordinate system. Here, in order to capture the true heterogeneous characteristics of a board cut from any location within a log, the important property tensors that exist within the transport equations need to be rotated according to an angle θ from the horizontal, to align the principal axes (see Fig. 1). This angle represents the angle of the wood grain in terms of how close, and from which location the board under consideration was cut relative to the centre of the tree. The angle obviously varies within the

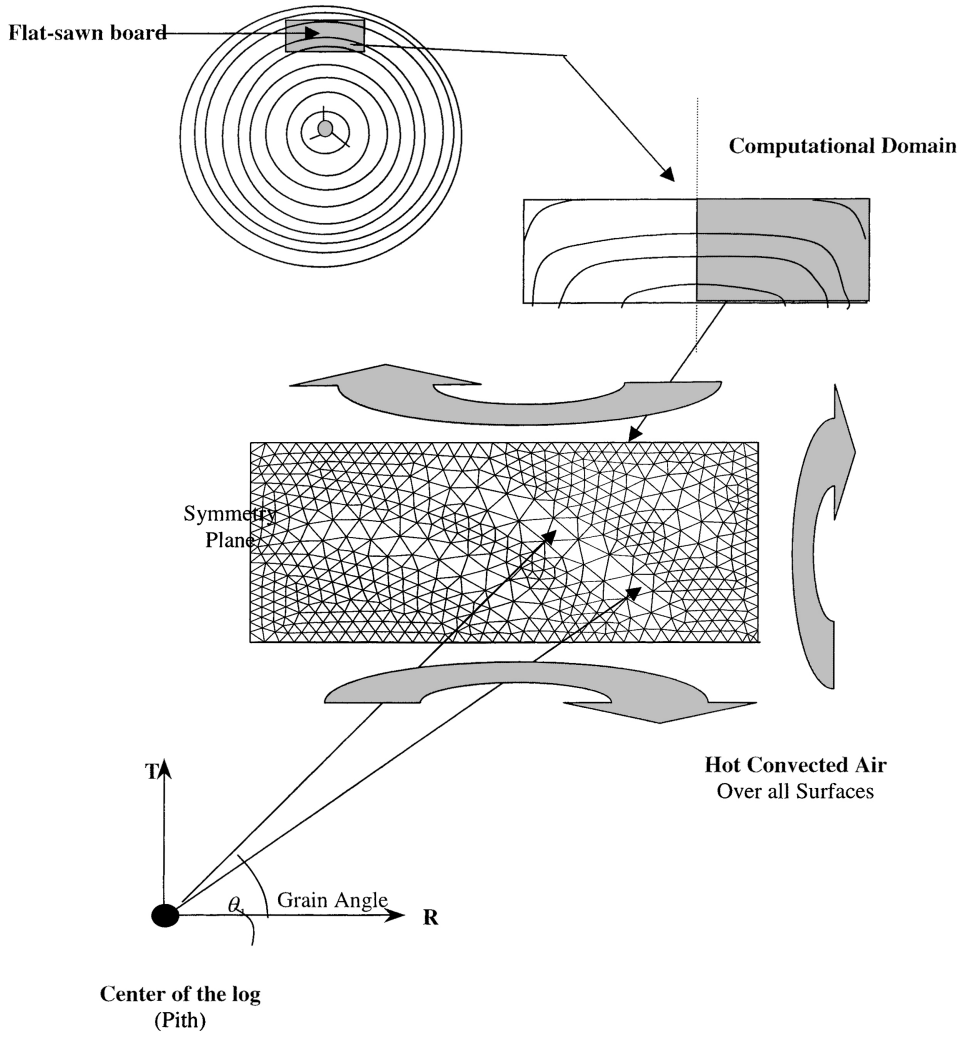

Fig. 1. Mesh generation and determination of the grain angle.

board section. As an example, the liquid permeability tensor becomes

$$\overline{\overline{\Lambda}}_{\mathrm{w}} = \boldsymbol{P}^{\mathrm{T}}\overline{\overline{\boldsymbol{K}}}^{*}_{\mathrm{w}}\overline{\overline{\boldsymbol{k}}}^{*}_{\mathrm{w}}\boldsymbol{P} \tag{8}$$

where $\boldsymbol{P}$ is the standard rotation transformation matrix and the star denotes the tensor evaluated in the material directions. It is important to emphasise that, due to the particular pore morphology of wood, the relative permeability is here a second order tensor rather than a scalar function. Consequently, the global permeability tensor has to be calculated as a matrix multiplication only in a co-ordinate system defined by the material directions (superscript "$*$" in Eq. (8)). Note that throughout this section, only global tensors, e.g. $\overline{\overline{\Lambda}}_{\mathrm{w}}$, expressed in the actual co-ordinate system will be used.

The mesh that is used for the computations is generated by specifying internal boundaries within the medium that correspond with the locations of the growth rings within the wood sample. The mesh is refined around these virtual growth ring locations. The density varies across the virtual growth rings according to experimental data [7]. Once the features of the wood sample have been captured, the domain is tessellated with triangles using the mesh generation software Easymesh. It should be noted that the net result of the mesh generation phase is a geometrical description of the virtual wood sample that has a wood density and grain angle associated with each triangle within the mesh. An example mesh of a virtual wood sample, together with the density variation across the growth rings is exhibited in Fig. 2, which uses 1000 elements. It is evident from this mesh that the density is lowest (light shading) for earlywood and highest (dark shading) for latewood.

2.6. The CV-FE discretisation procedure

The CV-FE discretisation process is derived for the liquid conservation law given in Eq. (1). The discretisation

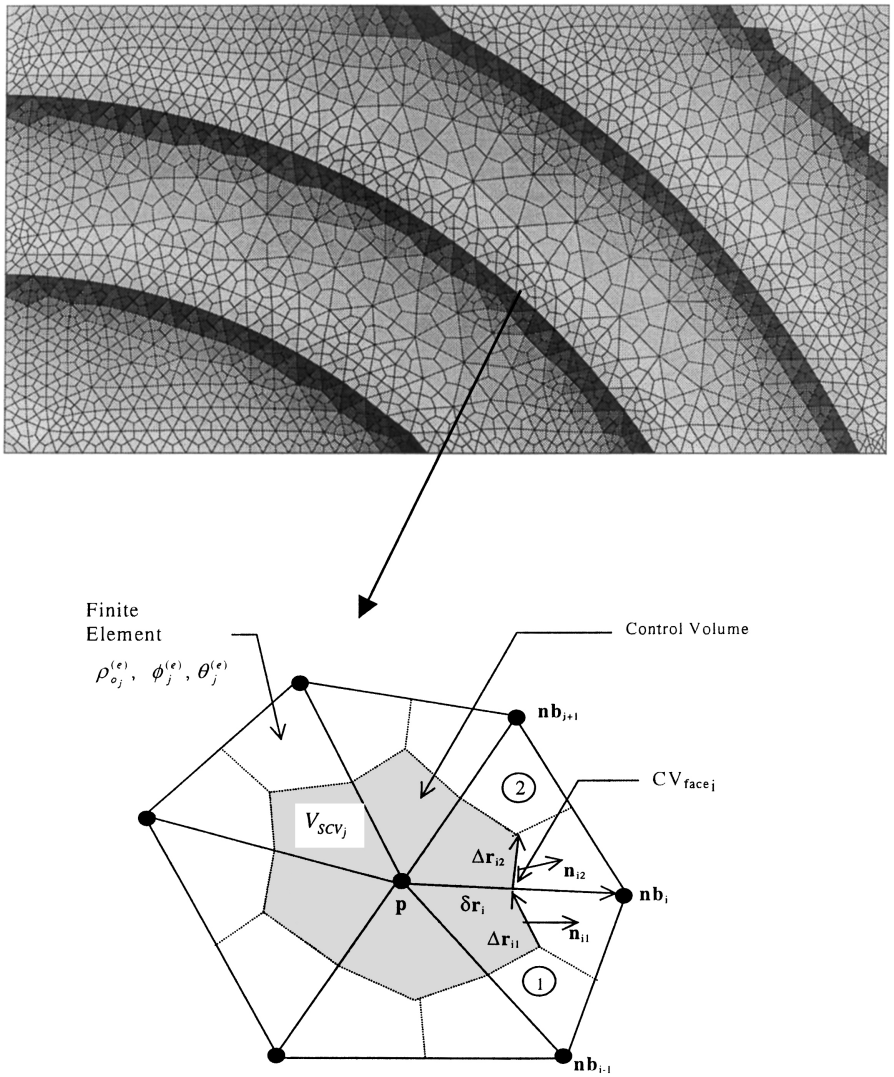

Fig. 2. Mesh structure, including the control-volumes built around each node. Dark shaded regions on the mesh represent latewood (high density) and light shaded regions represent earlywood (low density). The FE mesh is in black and the control-volumes is in white.

process proceeds by integrating the balance laws over control-volumes that are formed directly from the triangular mesh by joining the centroids of the triangles to the midpoints of the triangle vertices (see Fig. 1). After integrating over each control-volume within the computational domain, a system of non-linear equations result whereby each equation within this system can be cast into a discrete analogue of the conservation equation:

$$F_{\mathrm{w}}(\boldsymbol{u}_p) \equiv \frac{\Delta V_p}{\delta t}(\Psi_{\mathrm{w}_p}^{n+1} - \Psi_{\mathrm{w}_p}^{n}) - \sum_{i\in \mathrm{Nb}_p}\sum_{j=1}^{2}(\boldsymbol{J}_{\mathrm{w}}\cdot\hat{\boldsymbol{n}})_{\mathrm{CV}_{\mathrm{face}_{ij}}}||\Delta \boldsymbol{r}_{ij}|| = 0,$$

$$\text{where}\quad \boldsymbol{J}_{\mathrm{w}} = \frac{\overline{\overline{\Lambda}}_{\mathrm{w}}}{\mu}\rho_{\mathrm{w}}\nabla\varphi_{\mathrm{w}} + \frac{\overline{\overline{\Lambda}}_{\mathrm{g}}}{\mu}\rho_{\mathrm{v}}\nabla\varphi_{\mathrm{g}} + \overline{\overline{\boldsymbol{D}}}_{\mathrm{eff}}\rho_{\mathrm{g}}\nabla\omega_{\mathrm{v}} + \overline{\overline{\boldsymbol{D}}}_{\mathrm{b}}\nabla\bar{\rho}_{\mathrm{b}} \tag{9}$$

In Eq. (9), the term Ψ_{w} represents the conserved quantity of total liquid, $\Psi_{\mathrm{w}} = \rho_0(x)X + \varepsilon_{\mathrm{g}}\rho_{\mathrm{v}}$. Nb_p denotes the set of neighbouring points that surround node p. The internal sum over the index j indicates that there are two sub-control-volume faces, one from each of the two adjacent triangular elements that share the vector $\delta\boldsymbol{r}_i$ along a common edge, to be treated for each CV face (see Fig. 1). The tensor terms in this equation within the flux expression are complicated functions of the state system variables. Because Eq. (9) requires expressions for the discrete form of the flux in the normal direction to the CV face, it becomes necessary to approximate all of the gradient terms. If $N_k^j(x, y)$ are the usual Lagrange polynomial C^0 basis functions then the gradient for the jth element associated with the $\mathrm{CV}_{\mathrm{face}_i}$ can be written as $(\nabla\phi)_j = \sum_k \nabla N_k^j \phi_k^j$. This expression, after some manipulations, can be cast in the following compact matrix form (see [11] for further details):

$$(\nabla\phi)_j = \boldsymbol{G}_j\,\mathrm{d}\phi_j \tag{10}$$

Substituting Eq. (10) where appropriate into Eq. (9) gives the following discrete form of the flux through the $\mathrm{CV}_{\mathrm{face}_{ij}}$:

$$\begin{aligned}(\boldsymbol{J}_{\mathrm{w}}\cdot\hat{\boldsymbol{n}})_{\mathrm{CV}_{\mathrm{face}_{ij}}} = {} & \mathrm{d}\varphi_{\mathrm{w}_j}^{\mathrm{T}}\boldsymbol{G}_j^{\mathrm{T}}(\overline{\overline{\lambda}}_{\mathrm{w}})_{\mathrm{CV}_{\mathrm{face}_{ij}}}\hat{\boldsymbol{n}}_{ij}(\rho_{\mathrm{w}})_{\mathrm{CV}_{\mathrm{face}_i}} \\ & + \mathrm{d}\varphi_{\mathrm{g}_i}^{\mathrm{T}}\boldsymbol{G}_j^{\mathrm{T}}(\overline{\overline{\lambda_{\mathrm{g}}}})_{\mathrm{CV}_{\mathrm{face}_{ij}}}\hat{\boldsymbol{n}}_{ij}(\rho_{\mathrm{v}})_{\mathrm{CV}_{\mathrm{face}_i}} \\ & + \mathrm{d}\omega_{\mathrm{v}_j}^{\mathrm{T}}\boldsymbol{G}_j^{\mathrm{T}}(\overline{\overline{D}}_{\mathrm{v}})_{\mathrm{CV}_{\mathrm{face}_{ij}}}\hat{\boldsymbol{n}}_{ij}(\rho_{\mathrm{g}})_{\mathrm{CV}_{\mathrm{face}_{ij}}} \\ & + \mathrm{d}\bar{\rho}_{\mathrm{b}_j}^{\mathrm{T}}\boldsymbol{G}_j^{\mathrm{T}}(\overline{\overline{D}}_{\mathrm{b}})_{\mathrm{CV}_{\mathrm{face}_{ij}}}\hat{\boldsymbol{n}}_{ij}\end{aligned} \tag{11}$$

where it has been taken into consideration that the global tensor terms are symmetric. The unit normal vector is given by $\hat{\boldsymbol{n}}_{ij} = (-\Delta y_{ij}, \Delta x_{ij})^{\mathrm{T}}/||\Delta\boldsymbol{r}_{ij}||$. Note that a term like $(\overline{\overline{\lambda}}_{\mathrm{w}})_{\mathrm{CV}_{\mathrm{face}_{ij}}}$ implies evaluation of the components of the liquid mobility tensor at the CV face. The evaluation of all of the tensor terms is important to the accuracy of the finite volume scheme and is discussed further in the next section.

2.7. Evaluation of the tensor terms at the CV face

As can be seen from Eq. (11), it is necessary to define spatial averaging techniques for the evaluation of the tensor terms at the control-volume faces. Typically, the diffusion tensors $\overline{\overline{\boldsymbol{D}}}_{\mathrm{eff}}$ and $\overline{\overline{\boldsymbol{D}}}_{\mathrm{b}}$ are averaged at the CV face by using arithmetic averaging for their components $d_{ij\,\mathrm{CV}_{\mathrm{face}_i}} = (1/2)(d_{ij\,p} + d_{ij\,\mathrm{Nb}_i})$.

The correct treatment of the advection and convection terms within the discrete conservation laws is essential to the accuracy and performance of the numerical scheme and ensures that smearing of the drying fronts can be avoided [14,15]. In TransPore, the spatial weighting scheme adopted to treat these terms concerns flux limiting. This strategy, although much more complicated than first-order upstream weighting, provides excellent results in reducing numerical dispersion. Such techniques allow coarse meshes to be employed for the simulations whilst still allowing accurate results to be produced (see [14] for further details).

2.8. Computation of the wood density at a node

Recall that each control-volume shares sub-control-volumes that belong to a triangular finite-element (see Fig. 2). Each of these finite-elements has associated with it an angle and a density. The apparent density needs to be determined at a node so that it can be used for the finite volume conservation equations. In this work, an area weighted averaging technique is used based on the following formula:

$$\rho_0(\boldsymbol{x}_p) = \frac{\sum_{j\in\mathrm{Nb}_p} A_{\mathrm{SCV}\,j}^{(\mathrm{e})}\rho_{0j}^{(\mathrm{e})}}{\sum_{j\in\mathrm{Nb}_p} A_{\mathrm{SCV}_j}^{(\mathrm{e})}} \tag{12}$$

where $\boldsymbol{x}_p$ represents the position vector of the node at the vertex-centre of the control-volume. The quantities $\sum_{j\in\mathrm{Nb}_p} A_{\mathrm{SCV}_j}^{(\mathrm{e})}\rho_{0j}^{(\mathrm{e})}$ and $\sum_{j\in\mathrm{Nb}_p} A_{\mathrm{SCV}_j}^{(\mathrm{e})}$ represent the solid mass and the total area of the control-volume, respectively. The porosity $\phi(\boldsymbol{x}_p)$ can be computed for each control-volume once the apparent density from Eq. (12) is known:

$$\phi(\boldsymbol{x}_p) = 1 - \frac{\rho_0(\boldsymbol{x}_p)}{\rho_{\mathrm{s}}}, \quad \rho_{\mathrm{s}} = 1530\,\mathrm{kg\,m^{-3}} \tag{13}$$

where ρ_{s} is the density of the cell wall substance.

2.9. Determination of the initial moisture content distribution

The initial moisture content field has to be computed prior to the commencement of the drying process. The average moisture content of the wood sample will initially be supplied to the code and it is from this value that the initial distribution can be determined. An important correlation needed for determining the initial moisture content field is the capillary pressure relation, which varies with liquid

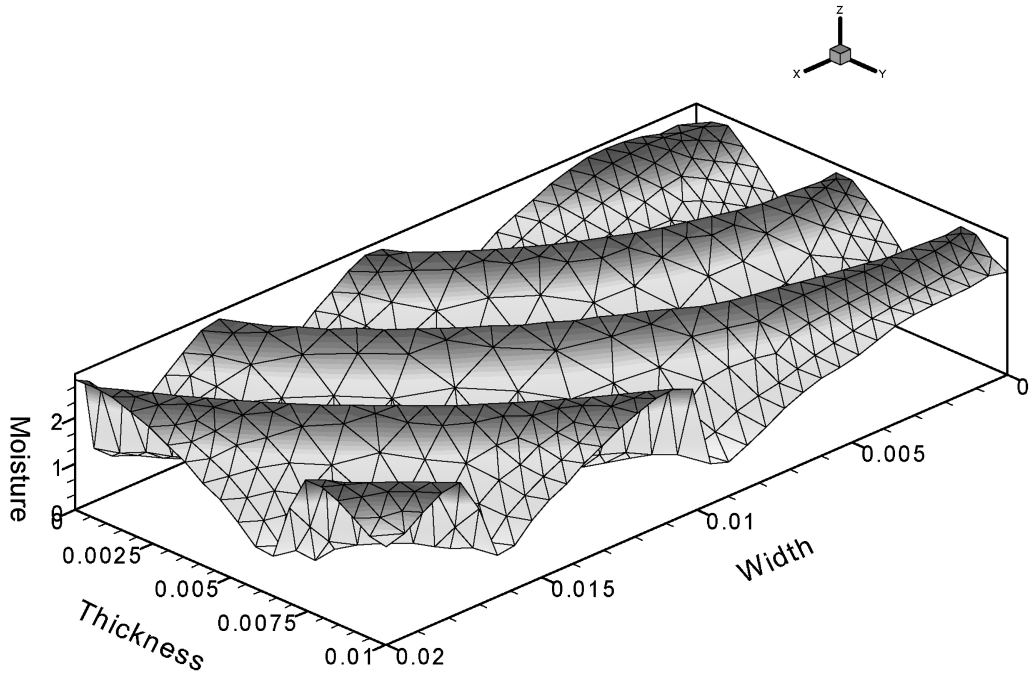

Fig. 3. Initial moisture content field deduced according to the density variation across the growth rings and the initial average moisture content.

saturation, temperature and density. Typically, the pores in the latewood component of the annual ring are smaller than in the earlywood component. Consequently, stronger capillary forces become evident in latewood. The mathematical expression postulated from image analysis performed on different locations within the annual ring of spruce by Perré [6] has been used to model this phenomenon.

By noting further that all capillary forces must be in equilibrium when the medium is in its initial state, the capillary pressures at each node of the computational mesh must be equal. Let P_{c0} be this equilibrium capillary pressure, then the following equation must hold for each control-volume:

$$P_{c_p}(S_w, T, \rho_0) = P_{c0}, \quad \forall\, p = 1, 2, \ldots, N \tag{14}$$

The moisture content for the control-volume is given by

$$X_p = \frac{\phi(\boldsymbol{x}_p) S_p \rho_w}{\rho_0(\boldsymbol{x}_p)} + X_{FSP} \tag{15}$$

Let the average moisture content be $\bar{X}$, then the equation that allows closure of this non-linear system is:

$$\frac{\sum_{p=1}^{N} A_p \rho_0(\boldsymbol{x}_p) X_p}{\sum_{p=1}^{N} A_p \rho_0(\boldsymbol{x}_p)} = \bar{X}, \quad A_p = \sum_{j \in \mathrm{Nb}_p} A_{\mathrm{SCV}_j} \tag{16}$$

The above non-linear system of $N + 1$ equations can be solved for the unknown initial saturations S_{w_p}, $p = 1, 2, \ldots, N$ at each node point and the equilibrium capillary pressure P_{c0} using the Newton method. This algorithm always succeeded in determining the initial moisture distribution. Once the initial saturation values are known at all node points, it is then possible to deduce the initial moisture field. Fig. 3 depicts the initial moisture distribution computed for a typical mesh. Clearly, the moisture is highest for the low density regions (earlywood) and lowest for the high density regions (latewood).

2.10. Solving the non-linear system

The non-linear function $F_w(\boldsymbol{u}_p)$ is a complicated expression of the state variable set $(X, T, \bar{\rho}_a)$ at the nodes p and all of the neighbouring nodes that surround the control-volume (CV_p) under consideration. The coefficients within expression (11) combine the non-linearities of the transport coefficients, which involve the state function set at the node p and the neighbouring nodes together with the relevant geometric factors for the control-volume face.

Once the non-linear functions have been assembled for each CV within the computational domain, the result is a system of non-linear equations of the form $F(\boldsymbol{u}) = 0$. The solution vector $\boldsymbol{u}$ contains the primary variables for each CV within the mesh. This system then must be resolved at each time step in order to advance all of the primary variables in time. A globally convergent Newton method is used to resolve this system [12,14].

3. Results and discussion

The simulation results using both the homogeneous and heterogeneous drying model formulations are reported for the drying of a small sample of softwood that contains four growth rings. All of the parameters used for the simulations

are listed in Table 1. Both low and high temperature drying conditions have been tested to exhibit the differences in the drying kinetics generated by the heterogeneous model in comparison to the existing homogeneous model.

The air velocity used for the simulations was $3\,m\,s^{-1}$, yielding heat and mass exchange coefficients of $25\,W\,m^{-2}\,K^{-1}$ and $0.025\,m\,s^{-1}$, respectively. Gravity is acting in the Transverse direction. The board sample is chosen to represent a flat-sawn section, so that the material angle ranges approximately between 45 and 90°, within the computed half part of the section.

Figs. 4 and 5 exhibit the spatial evolution of the moisture field, internal pressure distribution and temperature distribution at the centre plane of the wood sample for various times for low temperature drying conditions using the

Table 1
The drying conditions and initial material property data used in the simulations

Drying conditions and material properties	Values used for the computations
Average initial moisture content	170%
Initial temperature	30 °C
Average porosity	0.703
Average apparent density	$455\,kg\,m^{-3}$
Wood cross-section: RT directions	2 cm × 1 cm
Low temperature conditions (case 1)	Dry bulb, 60 °C; wet bulb, 40 °C
High temperature conditions (case 2)	Dry bulb, 140 °C; wet bulb, 80 °C

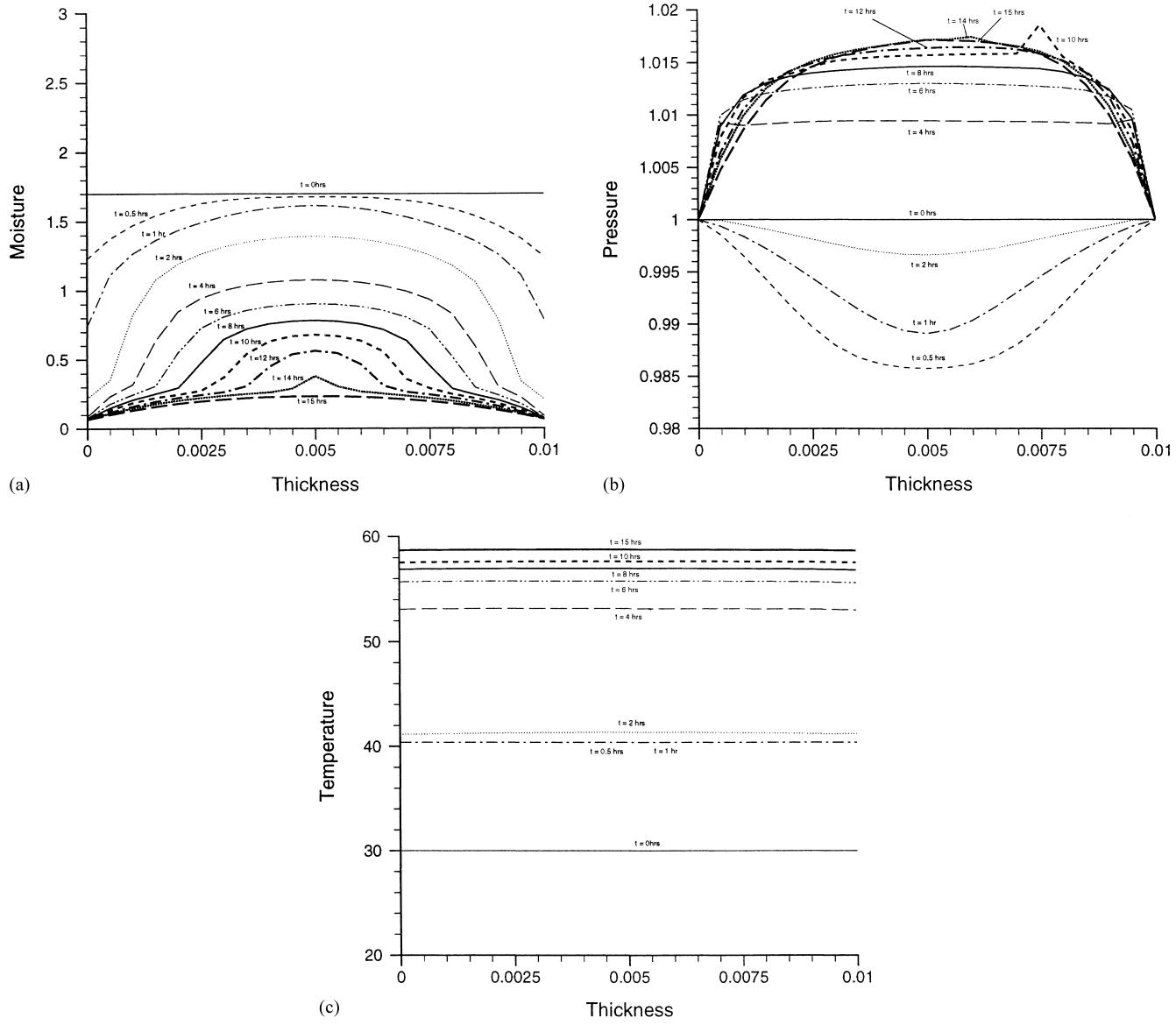

Fig. 4. Central plane moisture content (a), pressure (b), and temperature (c) field evolution for homogeneous model using low temperature drying conditions.

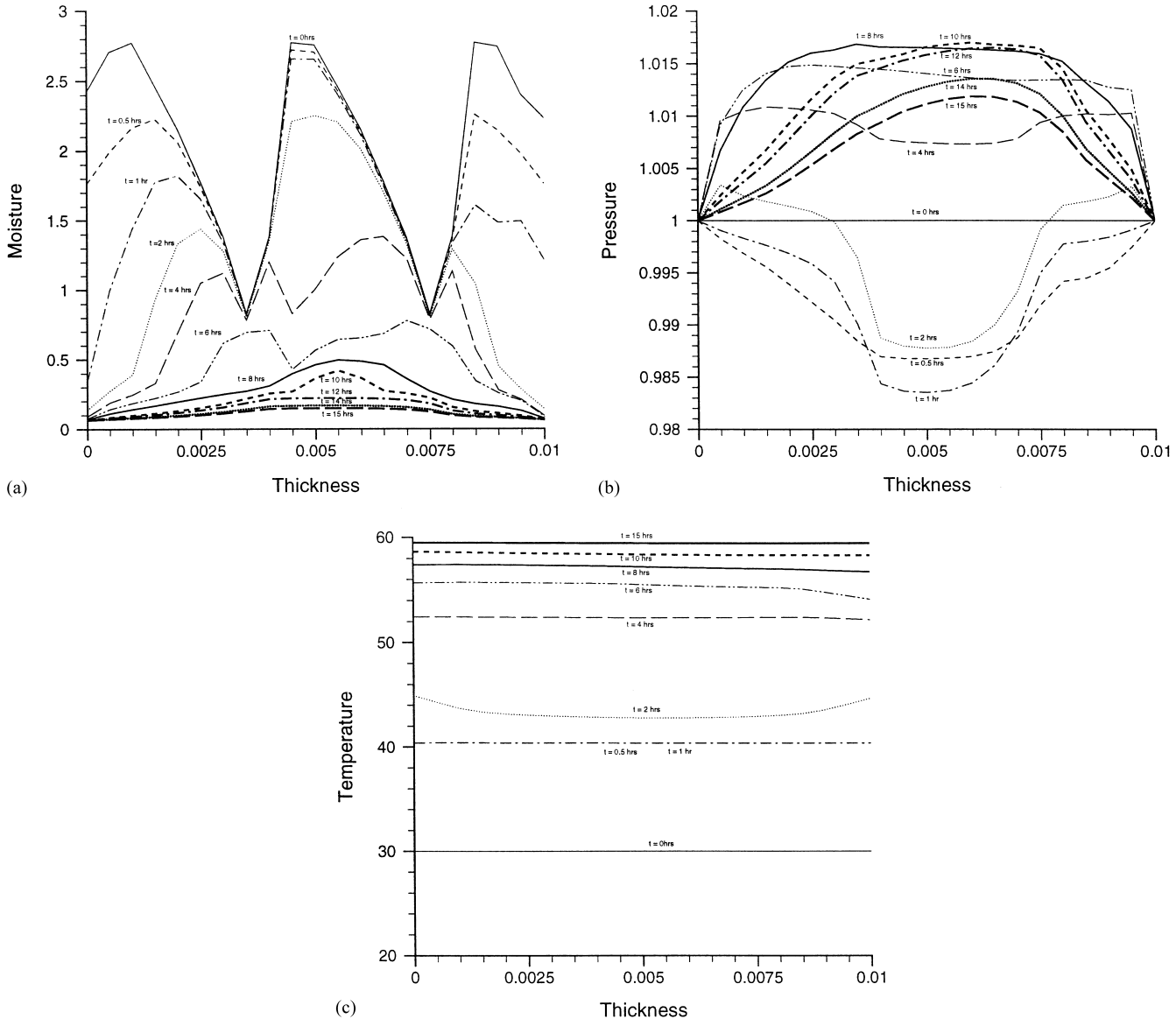

Fig. 5. Central plane moisture content (a), pressure (b), and temperature (c) field evolution for heterogeneous model using low temperature drying conditions.

homogeneous and heterogeneous models respectively. It is clear from these figures that there are substantial differences in the kinetics generated by the two models. The moisture content variation in space for the homogeneous model is classical, with just a slight effect of the material angle being evident and a smooth progression of the moisture content from its initial constant state to the equilibrium value established by the drying air characteristics. However, for the heterogeneous model, the behaviour is substantially different. In particular, the influence of the strong density variation across the growth rings can be observed clearly, with the moisture fields during the constant rate drying period being higher in the earlywood regions and lower in the latewood regions of the wood sample. As the drying proceeds, the earlywood locations tend towards the fibre saturation point at first and then the latewood locations attain this value. During the later stages of drying, when all of the free water has been removed from the tracheids of the wood, the process resembles that computed by the homogeneous model.

The pressure field computed by the homogeneous model is again classical. It exhibits an underpressure caused by the evacuation of water from the pores by capillarity during the constant rate drying period, followed by a steady increase in pressure until a small overpressure is evident within the medium during the falling rate drying period. The material angle again has only a minimal effect on the symmetry of the pressure profiles. It is thought that the unusual hump in the pressure curve at 10 h of drying is an artefact of the coarseness of the mesh. Such effects were not evident when the same computations were performed using a refined

mesh. The heterogeneous model results for the pressure distribution are given in Fig. 5b. It is clear that there are some differences to those computed by the homogeneous model, although the overall characteristics are similar. Interestingly, the prominent growth ring phenomena clearly evident in the moisture field are not as obvious for the pressure field. Nevertheless, the shape of the pressure curves in space during the constant rate period is definitely impacted by the non-uniform nature of the moisture extraction during the same period.

The temperature profiles, depicted in Figs. 4c and 5c for both models, are similar. The curves show a steady increase in temperature up to the wet bulb temperature of 40 °C during the constant rate drying period, followed by a climb to the dry bulb temperature of 60 °C. The impact of the growth rings on the wood sample temperature distribution is not at all obvious for this case.

The spatial evolution of the moisture field, internal pressure distribution and temperature distribution at the centre plane of the wood sample for various times using the homogeneous and heterogeneous models for high temperature drying conditions are exhibited in Figs. 6 and 7. For high temperature drying the overall kinetics are different to those discussed for case 1. The main difference being the large overpressure that is generated within the medium that enables a substantial reduction in the overall drying time in comparison with the low temperature drying case. For these harsh drying conditions, the wood sample is completely dry after only 3 h, as opposed to 15 h for the low temperature conditions. The moisture field again is completely different

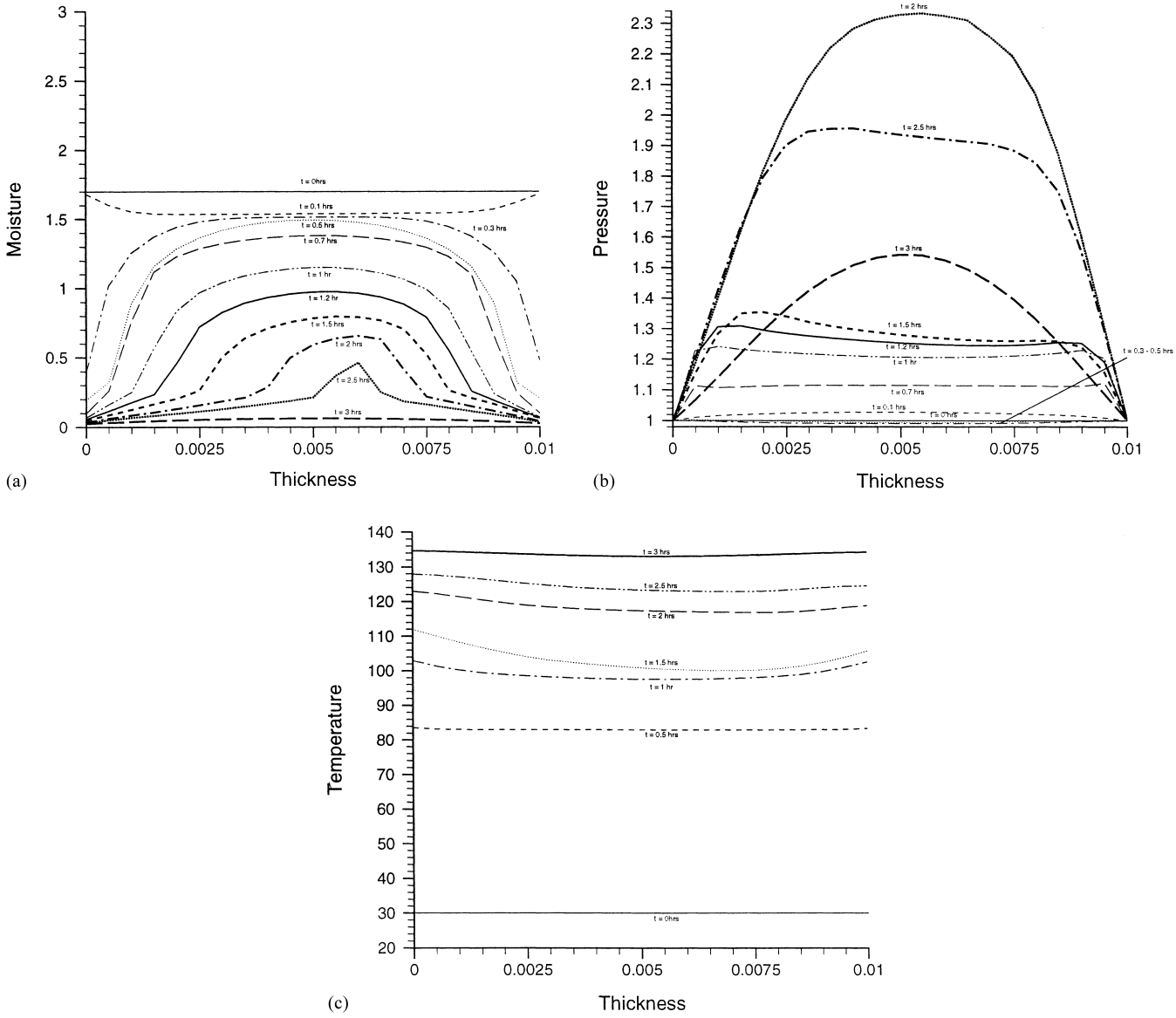

Fig. 6. Central plane moisture content (a), pressure (b), and temperature (c) field evolution for homogeneous model using high temperature drying conditions.

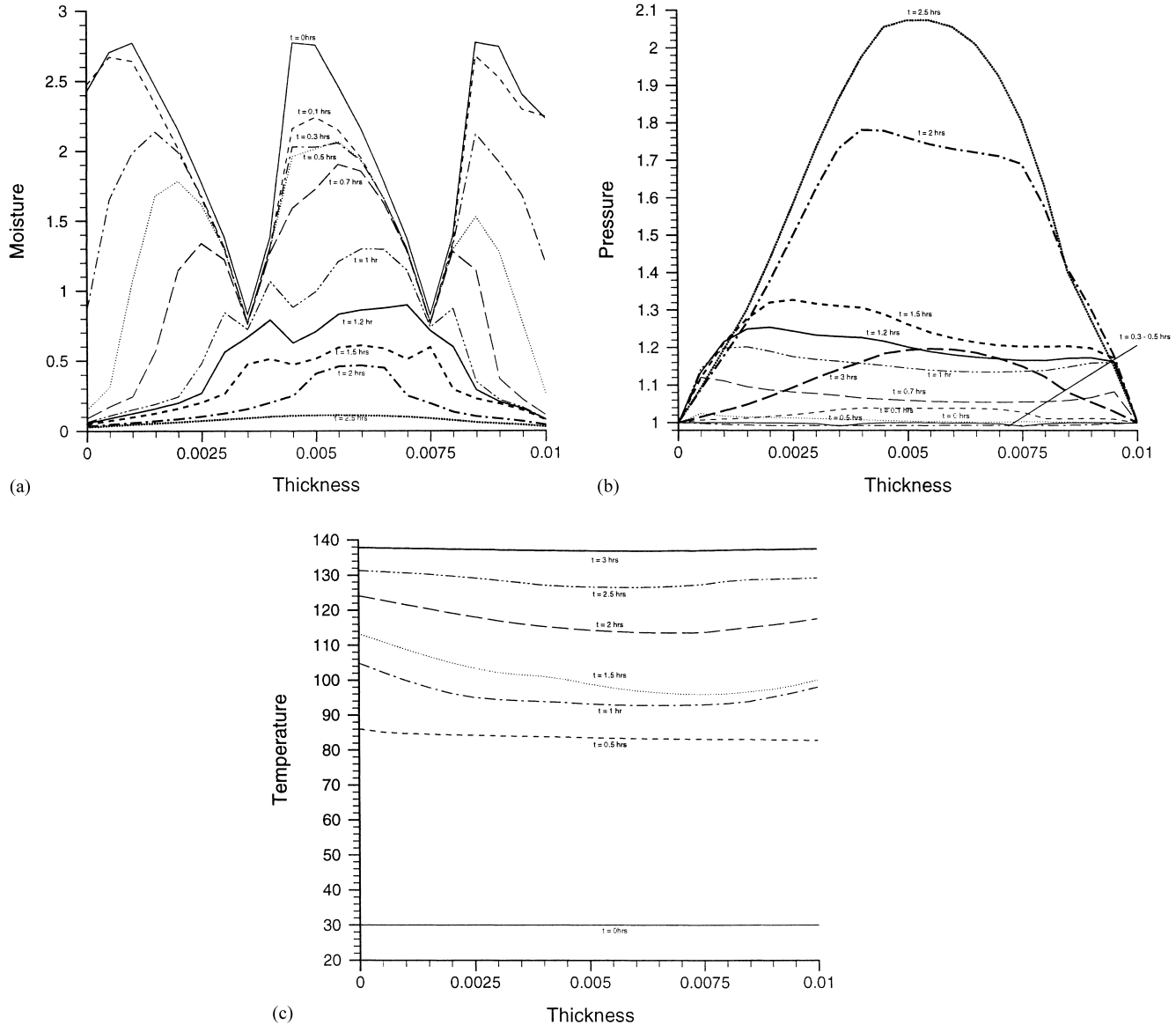

Fig. 7. Central plane moisture content (a), pressure (b), and temperature (c) field evolution for heterogeneous model using high temperature drying conditions.

for the heterogeneous model when compared with the homogeneous model, where it is again clear that the earlywood zones of the sample dry faster than the latewood zones. The impact of the growth rings on the temperature distribution again is also negligible.

Perhaps the best way to study the behaviour of the distributions of moisture content, internal pressure and temperature for the heterogeneous model (case 2 drying conditions) is via a series of carpet plots that display the drying characteristics of the wood sample at 0.3, 0.7, 1, 1.5 and 2.5 h of drying in Figs. 8–11. At 0.3 h, the falling rate drying period commences, the wood sample is dry at the two leading corners and the temperature begins to increase there. Water appears to move from the medium along the earlywood components of the growth rings. At 0.7 h, the latewood sections of the growth rings at the drying surface become dry and the temperature starts to increase. A small overpressure now is evident within the board. This alternation of dry and wet zones at the surface is typical of this heterogeneous material. This can explain, at the global scale, a progressive decrease of the drying rate, from the value given by the external drying conditions (first drying period) down to lower values controlled by internal mass transfer. At 1.5 h of drying, Only one zone remains wet. On the other part of the section, the temperature already increased above the boiling point of water: an important overpressure exists in the inner part of the section. At 2.5 h of drying, the entire section is within the hygroscopic range. All variable fields are now smoother and resemble what could be computed using a homogeneous model. An internal overpressure

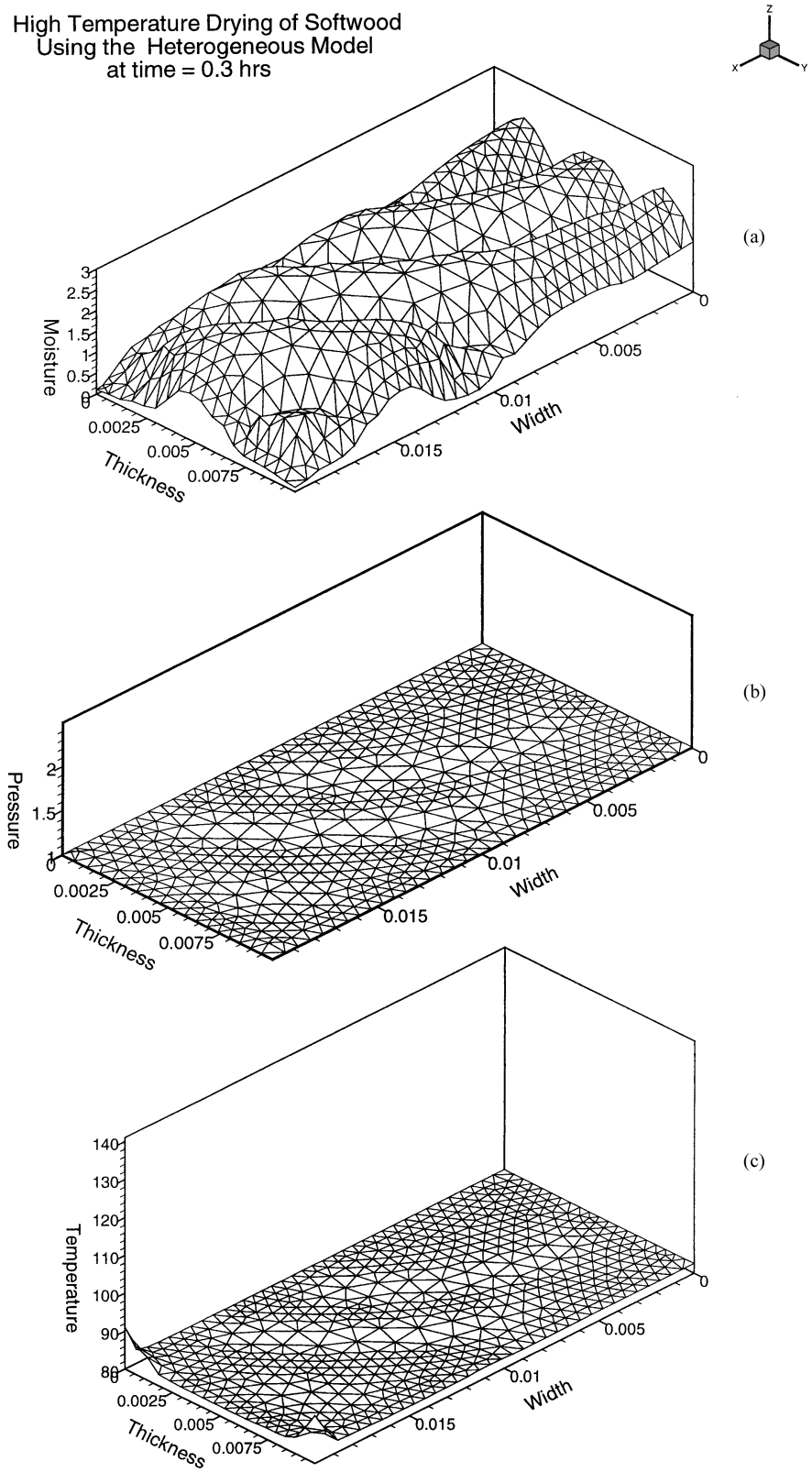

Fig. 8. Carpet plots depicting the moisture content (a), pressure (b), and temperature (c) distributions for high temperature drying after 0.3 h of drying.

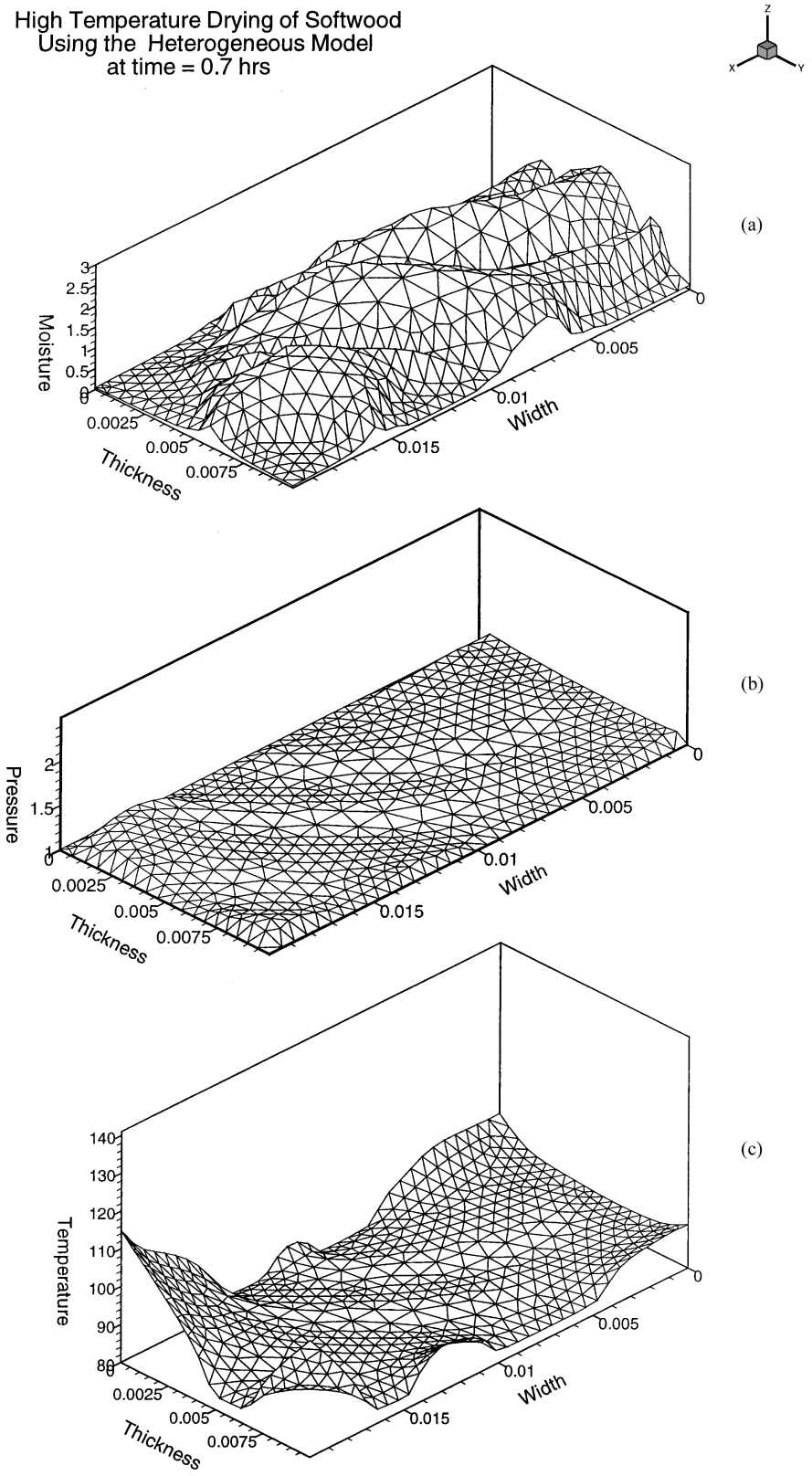

Fig. 9. Carpet plots depicting the moisture content (a), pressure (b), and temperature (c) distributions for high temperature drying after 0.7 h of drying.

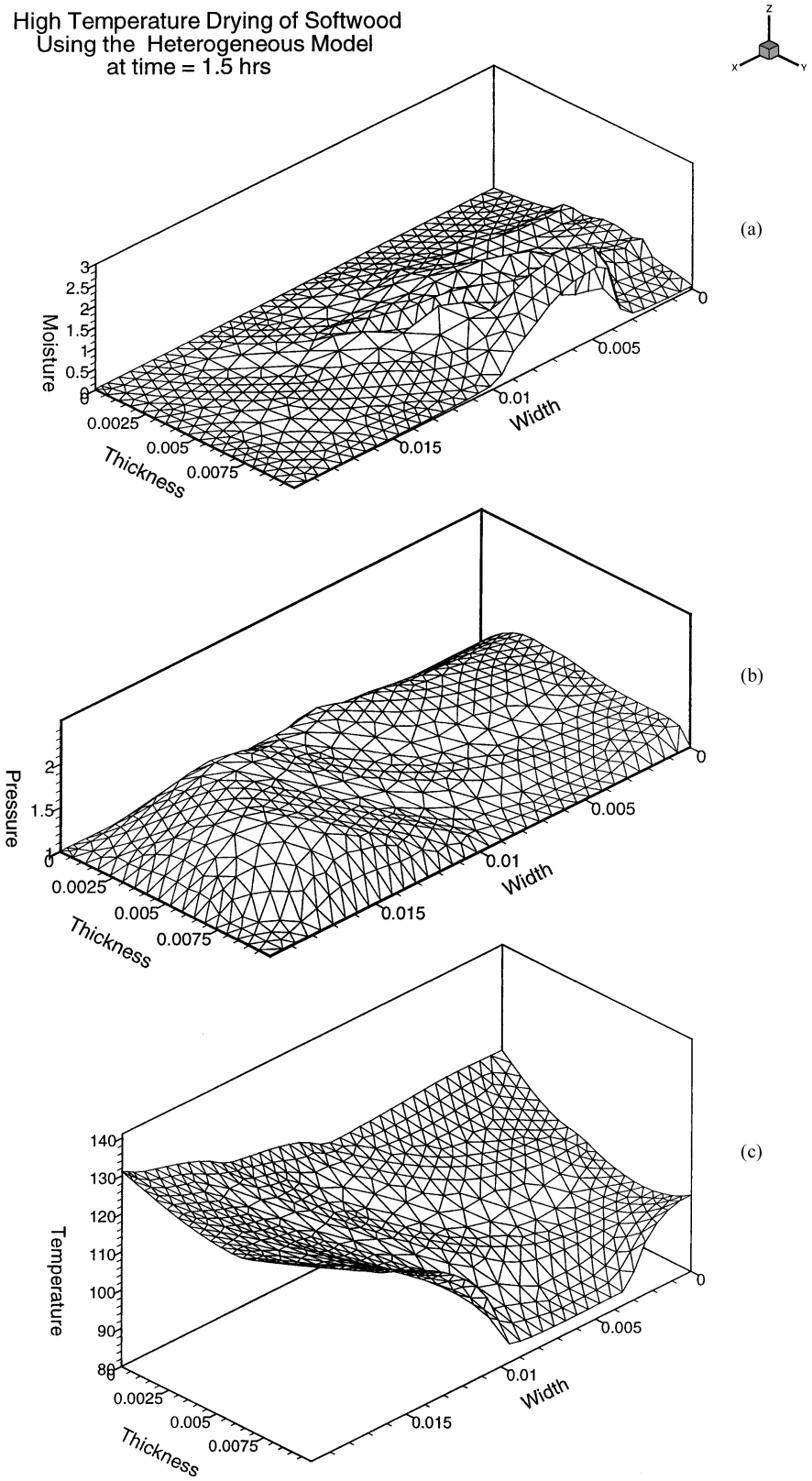

Fig. 10. Carpet plots depicting the moisture content (a), pressure (b), and temperature (c) distributions for high temperature drying after 1.5 h of drying.

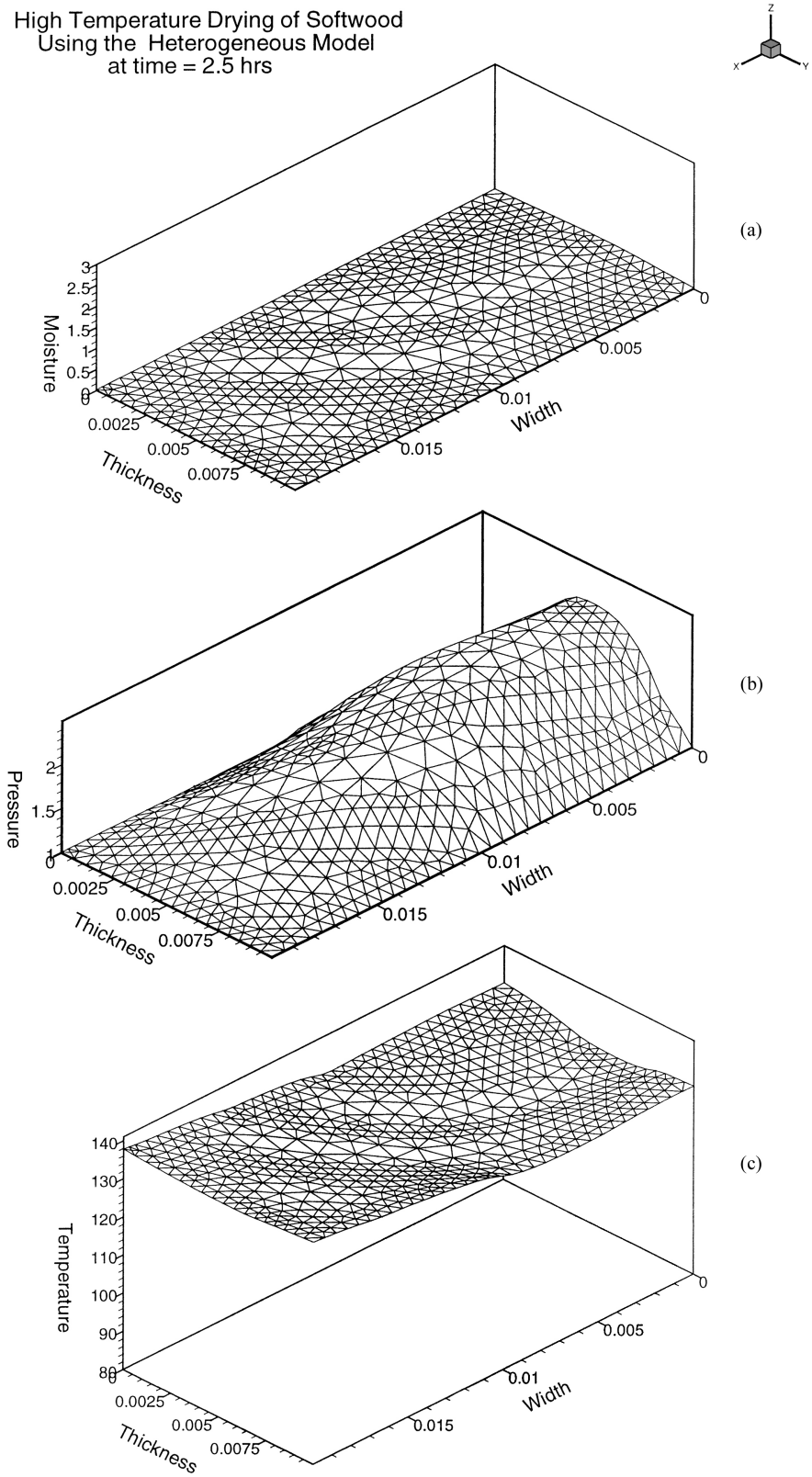

Fig. 11. Carpet plots depicting the moisture content (a), pressure (b), and temperature (c) distributions for high temperature drying after 2.5 h of drying.

still exits for a while, but the drying process is almost finished.

4. Conclusions

A completely new version of TransPore is presented in this work that allows spatial variations to be considered in both the anisotropy of the material directions and the transport properties according to the density. Moreover, the use of a CV-FE formulation ensures that any geometrical shape can be computed. The model enables the behaviour of the moisture content, internal temperature and pressure fields to be monitored during the drying process.

Such a comprehensive model is highly demanding in terms of computer resources (CPU time and memory) unless a suite of sophisticated numerical techniques is implemented to ensure both accurate and efficient simulation results. Using this tool, very novel physical phenomena become approachable. For example, it can be seen that the overpressure generated by high temperature convective drying is able to drive a moisture flux that follows the annual ring contour. This results from the most permeable part due to earlywood. Additional new possibilities are probably to be expected, for wood and also for other materials.

Acknowledgements

One of the Authors, Turner, would like to thank the French organisation INRA for funding his visit to the ENGREF/INRA laboratory to enable this work to be realised. The travel assistance offered under the Personal Development Program at the QUT should be acknowledged also. Both authors would like to acknowledge the use of the mesh generation software Easymesh written by Bojan Niceno (niceno@univ.trieste.it).

References

[1] J.F. Siau, Transport Processes in Wood, Springer-Verlag, 1984.
[2] P. Bonneau, J.R. Puiggali, Influence of heartwood–sapwood proportions on the drying kinetics of a board, J. Wood Sci. Technol. 28 (1993) 67–85.
[3] L. Gong, O.A. Plumb, The effect of heterogeneity on wood drying. Part I. Model development and predictions, J. Drying Technol. 12 (8) (1994) 1983–2001.
[4] L. Gong, O.A. Plumb, The effect of heterogeneity on wood drying. Part II. Experimental results, J. Drying Technol. 12 (8) (1994) 2003–2026.
[5] O.A. Plumb, Li. Gong, Modelling the effect of heterogeneity on wood drying, in: in: I.W. Turner, A.S. Mujumdar (Eds.), Mathematical Modeling and Numerical Techniques in Drying Technology, Marcel Dekker, New York, 1996, pp. 221–258, ISBN: 0-8247-9818-X.
[6] P. Perré, Image analysis, homogenization, numerical simulation and experiment as complementary tools to enlighten the relationship between wood anatomy and drying behavior, Drying Technol. J. 15 (9) (1997) 2211–2238.
[7] P. Perré, I.W. Turner, Determination of the material property variations across the growth ring of softwood for use in a heterogeneous drying model. Part I. Capillary pressure, tracheid model and absolute permeability, Holzforschung 55 (3) (2001) 318–323.
[8] S. Whitaker, Simultaneous heat, mass, and momentum transfer in porous media: a theory of drying, Adv. Heat Transfer 13 (1977) 119–203.
[9] S. Whitaker, Coupled transport in multiphase systems: a theory of drying, Adv. Heat Transfer 31 (1998) 1–104.
[10] P. Perré, I.W. Turner, The use of macroscopic equations to simulate heat and mass transfer in porous media, in: I.W. Turner, A.S. Mujumdar (Eds.), Mathematical Modeling and Numerical Techniques in Drying Technology, Marcel Dekker, New York, 1996, pp. 83–156, ISBN: 0-8247-9818-X.
[11] P. Perré, I. Turner, TransPore: a generic heat and mass transfer computational model for understanding and visualising the drying of porous media, invited paper, Drying Technol. J. 17 (7) (1999) 1273–1289.
[12] P. Perré, I. Turner, A 3D version of TransPore: a comprehensive heat and mass transfer computational model for simulating the drying of porous media, Int. J. Heat Mass Transfer 42 (24) (1999) 4501–4521.
[13] P. Perré, I.W. Turner, Determination of the material property variations across the growth ring of softwood for use in a heterogeneous drying model. Part II. Use of homogenisation to predict bound liquid diffusivity and thermal conductivity, Holzforschung 55 (4) (2001) 417–425.
[14] I.W. Turner, P. Perré, The use of implicit flux limiting schemes in the simulation of the drying process: a new maximum flow sensor applied to phase mobilities, J. Appl. Math. Modell. 25 (2001) 513–540.
[15] P.A. Forsyth, A.J.A. Unger, E.A. Sudicky, Non-equilibrium multiphase subsurface flow: an object oriented approach, Technical report CS-96-19, Department of Computer Science, University of Waterloo, Waterloo, 1996.